An inverse finite element method for beam shape sensing: theoretical framework and experimental validation

An inverse finite element method for beam shape sensing: theoretical framework and experimental validation

Marco Gherlone[1], Priscilla Cerracchio[1], Massimiliano Mattone[1], Marco Di Sciuva[1] and Alexander Tessler[2]

[1] Department of Mechanical and Aerospace Engineering—Politecnico di Torino, Corso Duca degli Abruzzi 24, I-10129 Torino, Italy

[2] Structural Mechanics and Concepts Branch—NASA Langley Research Center, Mail Stop 190, Hampton, VA 23681-2199, USA

E-mail: marco.gherlone@polito.it, priscilla.cerracchio@polito.it, massimiliano.mattone@polito.it, marco.disciuva@polito.it and Alexander.Tessler-1@nasa.gov

Abstract

Shape sensing, i.e., reconstruction of the displacement field of a structure from surface-measured strains, has relevant implications for the monitoring, control and actuation of smart structures. The inverse finite element method (iFEM) is a shape-sensing methodology shown to be fast, accurate and robust. This paper aims to demonstrate that the recently presented iFEM for beam and frame structures is reliable when experimentally measured strains are used as input data.

The theoretical framework of the methodology is first reviewed. Timoshenko beam theory is adopted, including stretching, bending, transverse shear and torsion deformation modes. The variational statement and its discretization with C^0-continuous inverse elements are briefly recalled. The three-dimensional displacement field of the beam structure is reconstructed under the condition that least-squares compatibility is guaranteed between the measured strains and those interpolated within the inverse elements.

The experimental setup is then described. A thin-walled cantilevered beam is subjected to different static and dynamic loads. Measured surface strains are used as input data for shape sensing at first with a single inverse element. For the same test cases, convergence is also investigated using an increasing number of inverse elements. The iFEM-recovered deflections and twist rotations are then compared with those measured experimentally. The accuracy, convergence and robustness of the iFEM with respect to unavoidable measurement errors, due to strain sensor locations, measurement systems and geometry imperfections, are demonstrated for both static and dynamic loadings.

Keywords: Timoshenko beam theory, shape sensing, frame structures, inverse finite element method, experimental strain

1. Introduction

A key capability to enable the development of smart structures is real-time estimation of the deformed shape using *in situ* strain measurements. This technology is commonly referred to as *shape sensing*. Aircraft wings with embedded conformal antennas and those with morphing capability require real-time shape sensing to provide feedback for their actuation and con-

trol systems [1–3]. For large deployable frame structures that carry antennas, accurate on-orbit shape estimation presents an attractive solution to increase communication quality [4–6]. Knowledge of the structural displacements also enables real-time reconstruction of structural strains and stresses, and the application of failure criteria for structural health assess-ment [7].

The computation of the displacement field is traditionally performed on the basis of *in situ* strain data measured in real time by a network of strain sensors. Due to their lightness, accuracy and ease of embedding, fiber Bragg grating (FBG) sensors have been extensively studied for smart structure applications. On the other hand, traditional strain gauges can be conveniently used to perform laboratory tests and for validation purposes [8–10].

Some authors have performed deformed shape estimation by using methods based on global or piece-wise continuous basis functions [8, 9, 11–15]. Basis-function methods make use of an *a priori* set of functions and proper weights which are determined using strain–displacement relationships and measured surface strains. Todd and Vohra [12] showed how the shear effect can be included for the beam problem. In many cases [8, 9, 13–15] mode shapes are used as basis functions. Other works are based on classical beam equations that are used to integrate discretely measured strains and to determine the deflection of a beam [10, 16, 17]. For example, Ko *et al* [17] proposed a one-dimensional scheme based on classical beam theory to evaluate the deflection and cross-sectional twist angle of an aircraft wing. Using a two-line strain-sensing system on the top surface of the wing, the curvature is obtained at discrete locations along the wing span (by knowing the axial surface strain and the distance of the measuring device from the neutral axis), then the deflection is evaluated by numerical integration. The cross-sectional twist angle is computed by considering the difference in the deflection of the two sensing lines. Jones *et al* [18] employed a least-squares formulation for shape sensing of a cantilevered plate, where FBG measured strains were fitted with a cubic polynomial. The strain field was then integrated to obtain the plate deflection according to classical bending assumptions. Mainc¸on and co-workers [19, 20] developed a finite element formulation, seeking the solution for displacements and loads simultaneously. Starting from measured displacements and strains and requiring *a priori* knowledge of the material properties and a subset of applied loading, the formulation results in a number of unknowns that is three times the number of degrees of freedom in the finite element discretization. Nishio *et al* [21] employed a weighted-least-squares formulation to reconstruct the deflection of a composite cantilevered plate with embedded optical fibers. In this approach, the compatibility between analytical and measured bending curvatures is enforced in a least-squares sense.

Many of the aforementioned algorithms require sufficiently accurate loading and/or elastic-inertial material information—the kind of data that are either unavailable or difficult to obtain outside a laboratory environment. Some of these approaches also require mode shape analysis (Foss and Haugse [8], Lively *et al* [9], Bogert *et al* [13], Rapp *et al* [14], Kim *et al* [15]) or global equilibrium conditions to be fulfilled (Mainc¸on [19, 20]). For these reasons, few of these methods are applicable for real-time shape sensing of aerospace structures. A well-suited algorithm for real-time monitoring should be computationally fast, robust with respect to inherent errors in the strain measurements and general enough to model complex structural topologies under a wide range of loadings, material systems and inertial/damping characteristics. Tessler and Spangler [7] developed an inverse finite element method (iFEM) for shear-deformable plate and shell structures. The formulation is based on a least-squares variational principle and allows full-field reconstruction of the three-dimensional displacement vector from measured surface strains. Because only strain–displacement relations are used in the formulation, both static and dynamic responses can be reconstructed without any *a priori* knowledge of loading, material, inertial or damping structural properties. An experimental assessment of the method was presented in [22, 23], where the deformed shape of a slender beam was reconstructed by an iFEM shell model using FBG strain measurements. Recently, Gherlone *et al* [24–29] presented an iFEM formulation for shear-deformable beam and frame structures. Beam and frame shape-sensing analyses were performed for static and dynamic loadings using strain data from high-fidelity FE models. An application of the beam-iFEM approach to experimentally measured strains has been presented by Gherlone *et al* [28], who used low-fidelity iFEM discretizations to reconstruct accurate deflections and twist rotations of a statically loaded cantilevered beam.

This paper presents a brief review of the iFEM variational formulation which incorporates experimentally measured strains within a simple inverse-beam-frame element. The element is based on Timoshenko beam theory which includes the axial, bending, torsion and transverse shear deformations. Some experimental tests are then presented and discussed in which a thin-walled cantilevered beam is subjected to static and dynamic loadings. The experimentally measured strain data are used within a single inverse-beam element to model the entire beam. Alternatively, by applying linear regression to the available strain measurements, axially-distributed strain data are obtained; therefore, the new set of surface strains is used within higher-fidelity discretization models. To verify the accuracy of the methodology, the iFEM-predicted dis-placements and rotations are compared with those measured experimentally by displacement transducers distributed along the beam's span (for the static load cases) and recovered by means of an accelerometer (for the dynamic load cases). The accuracy achieved in all the tests demonstrates that this method is robust with respect to various sources of errors that inevitably afflict laboratory experiments as well as real applications. These errors include measurement errors, but also uncertainty in the strain gauge positions, boundary conditions and geometry.

2. The inverse-beam finite element formulation

Consider an isotropic, straight beam-frame structural member of Young's modulus E, shear modulus G and Poisson ratio

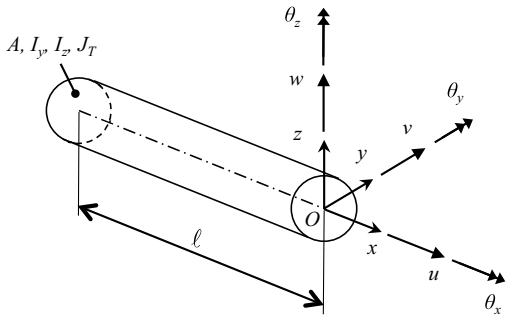

Figure 1. Beam geometry and kinematic variables.

ν (figure 1). The structural member is referred to a Cartesian coordinate system (x, y, z), where x is positioned along the centroidal and shear axis, and y and z are the cross-section's principal inertial axes. The frame member has length ℓ and its cross-section has area A, second moments of area with respect to the y- and z-axes I_y and I_z , respectively, and torsion constant J_{T} (figure 1).

Consistent with the hypotheses of Timoshenko beam theory (each cross-section remains flat and rigid with respect to thickness-stretch deformations along the y- and z-axes) [30] and neglecting axial warping due to torsion, the displacement field may be written as follows:

$$\begin{aligned} u_x(x, y, z) &= u(x) + z\theta_y(x) - y\theta_z(x) \\ u_y(x, y, z) &= v(x) - z\theta_x(x) \\ u_z(x, y, z) &= w(x) + y\theta_x(x) \end{aligned} \tag{1}$$

where u_x , u_y , and u_z are the displacements along the x-, y-, and z-axes respectively; u, v, and w are the corresponding average displacements; θ_x , θ_y , and θ_z are the rotations about the three coordinate axes. The *kinematic variables*, $\mathbf{u} \equiv [u,\ v,\ w,\ \theta_x\ ,\ \theta_y\ ,\ \theta_z\ ]^{\mathrm{T}}$, and their positive orientations are shown in figure 1. The displacement field, equation (1), gives rise to the linear strains

$$\begin{aligned} \varepsilon_x(x, y, z) &= e_1(x) + z\, e_2(x) + y\, e_3(x) \\ \gamma_{xz}(x, y) &= e_4(x) + y\, e_6(x) \\ \gamma_{xy}(x, z) &= e_5(x) - z\, e_6(x) \end{aligned} \tag{2}$$

where the *section strains* $\mathbf{e}(\mathbf{u}) \equiv [e_1,\ e_2,\ e_3,\ e_4,\ e_5,\ e_6]^{\mathrm{T}}$ are given by

$$\begin{aligned} e_1(x) &\equiv u_{,x}(x) & e_4(x) &\equiv w_{,x}(x) + \theta_y(x) \\ e_2(x) &\equiv \theta_{y,x}(x) & e_5(x) &\equiv v_{,x}(x) - \theta_z(x) \\ e_3(x) &\equiv -\theta_{z,x}(x) & e_6(x) &\equiv \theta_{x,x}(x). \end{aligned} \tag{3}$$

The inverse finite element method (iFEM) reconstructs the deformed structural shape by minimizing a weighted least-squares functional Φ containing the section strains obtained by *in situ* strain measurements, $\mathbf{e}^{\varepsilon}$, and $\mathbf{e}(\mathbf{u})$ defined by equations (3), i.e.,

$$\Phi(\mathbf{u}) = \|\mathbf{e}(\mathbf{u}) - \mathbf{e}^{\varepsilon}\|^2. \tag{4}$$

The kinematic variables $\mathbf{u}$ are then discretized within a finite element framework based on C^0-continuous shape functions, $\mathbf{N}(x)$,

$$\mathbf{u}(x) \simeq \mathbf{u}^h(x) = \mathbf{N}(x)\, \mathbf{q}^h \tag{5}$$

where $\mathbf{q}^h$ denotes the nodal degrees of freedom of the element. Consequently, the total least-squares functional is a sum of the N individual element contributions, $\Phi^e(\mathbf{u}^h,\ \mathbf{e}^{\varepsilon})$, i.e., $\Phi = \sum_{e=1}^{N} \Phi^e$. Accounting for the axial stretching, bending, twisting, and transverse shearing, the element functional Φ^e is given by the dot product of the weighting coefficients vector, $\mathbf{w}^e \equiv \{w_k^e\} = \{1,\ (I_y^e/A^e),\ (I_z^e/A^e),\ 1,\ 1,\ (J_{\mathrm{T}}^e/A^e)\}$, and the least-squares component vector, $\mathbf{\Phi}^e \equiv \{\Phi_k^e\}$, $(k = 1, \ldots, 6)$, [29]

$$\Phi^e(\mathbf{u}^h,\ \mathbf{e}^{\varepsilon}) \equiv \sum_{k=1}^{6} w_k^e \Phi_k^e \tag{6}$$

where A^e, I_y^e, I_z^e, and J_{T}^e are, respectively, the cross-section area, second moments of area with respect to the y- and z-axes, and torsion constant of the element cross-section. The six components of the element functional are given as the Euclidean norms

$$\Phi_k^e \equiv \frac{\ell^e}{n} \sum_{i=1}^{n} \left[e_{k(i)}(\mathbf{u}^h) - e_{k(i)}^{\varepsilon}\right]^2 \qquad (k = 1, \ldots, 6) \tag{7}$$

where ℓ^e is the element length, n is the number of locations where the section strains are evaluated (with axial coordinate x_i , $0 \le x_i \le \ell^e$), $e_{k\ (i)}^{\ \varepsilon}$ denotes the kth section strain that is computed from the measured strains (experimental values) at x_i , and $e_{k(i)}$ indicates the kth section strain interpolated within the element and evaluated at the same location. Invoking equations (3) and (5), the analytic element-level section strains are expressed in matrix form as

$$\mathbf{e}(\mathbf{u}^h) = \mathbf{B}(x)\mathbf{q}^h \tag{8}$$

where the matrix $\mathbf{B}(x)$ contains derivatives of the shape functions $\mathbf{N}(x)$ [29].

Substituting equation (8) into equation (7) and minimizing the element functional with respect to $\mathbf{q}^h$ results in the element matrix equation $\mathbf{a}^h\ \mathbf{q}^h = \mathbf{b}^h$, where the matrix $\mathbf{a}^h$ depends on the strain-gauge locations, x_i, and their number, n, whereas the vector $\mathbf{b}^h$ incorporates the corresponding strain values [29]. The usual finite element assembly of element contributions of a discretized structure, consistent with appropriate displacement transformations from an element (local) to a global coordinate system, is then performed by prescribing problem-specific displacement boundary conditions. The resulting system of equations has the form

$$\mathbf{A}\,\mathbf{q} = \mathbf{b} \tag{9}$$

where $\mathbf{A}$ is a non-singular system matrix provided that at least a minimum number of strain-gauge points, $n = n_{\min}$, is used, i.e., $n_{\min} = 1$ and 2, respectively, for constant and linearly distributed element section strains.

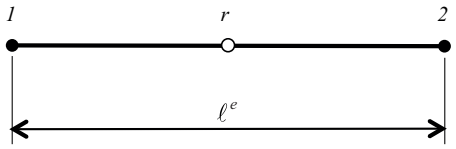

Figure 2. Inverse finite element geometry and nodes.

Solutions of equation (9) for the displacement degrees-of-freedom, **q**, are efficient. The matrix **A** is inverted only once because it remains unchanged for a given distribution of strain sensors and is independent of the measured strain values. The **b** vector, however, is dependent on the measured strain values; thus, at any strain measurement update during deformation, the matrix–vector multiplication, $\mathbf{A}^{-1}\,\mathbf{b}$, gives rise to the unknown degrees-of-freedom vector, **q**.

For frame structural elements loaded only by forces and moments at the end points, the section strains can be shown to exhibit the following span-wise distributions: e_1, e_4, e_5, and e_6 are constant, whereas e_2 and e_3 are linear [29]. From equation (3), it is deduced that u and θ_x are linear, θ_y and θ_z parabolic, v and w cubic. Thus, the following interpolations are adopted [29] (also refer to figure 2):

$$\begin{aligned}
u(x) &= \sum_{i=1,2} L_i^{(1)}(x)u_i,\\
\theta_x(x) &= \sum_{i=1,2} L_i^{(1)}(x)\theta_{xi}\\
\theta_y(x) &= \sum_{j=1,r,2} L_j^{(2)}(x)\theta_{yj},\\
\theta_z(x) &= \sum_{j=1,r,2} L_j^{(2)}(x)\theta_{zj}\\
v(x) &= \sum_{i=1,2} L_i^{(1)}(x)v_i - \sum_{j=1,r,2} N_j^{(3)}(x)\theta_{zj},\\
w(x) &= \sum_{i=1,2} L_i^{(1)}(x)w_i + \sum_{j=1,r,2} N_j^{(3)}(x)\theta_{yj}
\end{aligned} \tag{10}$$

where the subscripts 1, r and 2 denote positions along the beam length at the left-end, middle, and right-end node, respectively; $L_i^{(1)}(x)$ $(i = 1, 2)$ are linear Lagrange polynomials; $L_j^{(2)}(x)$ $(j = 1, r, 2)$ are quadratic Lagrange polynomials. The cubic polynomials $N_j^{(3)}(x)$ $(j = 1, r, 2)$ are obtained from standard cubic Lagrange polynomials by forcing the transverse shear section strains (e_4 and e_5) to be constant along the element. Refer to appendix A for the expression of $L_i^{(1)}(x)$, $L_j^{(2)}(x)$, and $N_j^{(3)}(\xi)$. The element has fourteen degrees of freedom: six at each end node plus the rotations θ_{yr} and θ_{zr} at the mid-span. By solving the element system of equations $\mathbf{a}^h\mathbf{q}^h = \mathbf{b}^h$ exactly with respect to the external degrees-of-freedom, the two internal rotation degrees-of-freedom are condensed, yielding a two-node/twelve-degrees-of-freedom element topology.

A key step in the formulation is to compute the section strains, $\mathbf{e}^\varepsilon$, from the experimentally measured surface strains. We shall restrict the present analysis to the beam-frame members with circular cross-sections only, and employ the

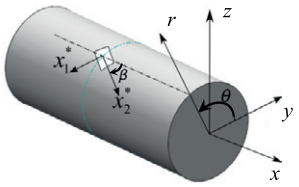

Figure 3. Orthogonal and cylindrical coordinate systems and strain gauge location and coordinates.

cylindrical coordinate system (θ, x, r) shown in figure 3. A strain gauge is placed on the external surface ($r = R_{\text{ext}}$), at $x = x_i$ and at a circumferential angle θ, and oriented along the β angle (figure 3). The relationship between the measured strain $\varepsilon^\varepsilon = \varepsilon_2{}^*$ and the six section strains at $x = x_i$, $e_{k\ (i)}^{\ \varepsilon}$ $(k = 1, \ldots, 6)$, is [29]

$$\begin{aligned}
\varepsilon^\varepsilon(x_i, \theta, \beta) = {} & e^\varepsilon_{1(i)}(c_\beta^2 - \nu s_\beta^2) + e^\varepsilon_{2(i)}(c_\beta^2 - \nu s_\beta^2)s_\theta R_{\text{ext}}\\
& + e^\varepsilon_{3(i)}(c_\beta^2 - \nu s_\beta^2)c_\theta R_{\text{ext}} + e^\varepsilon_{4(i)}c_\beta s_\beta c_\theta\\
& - e^\varepsilon_{5(i)}c_\beta s_\beta s_\theta + e^\varepsilon_{6(i)}c_\beta s_\beta R_{\text{ext}}
\end{aligned} \tag{11}$$

where $c_\theta \equiv \cos\theta$, $s_\theta \equiv \sin\theta$, $c_\beta \equiv \cos\beta$, and $s_\beta \equiv \sin\beta$. For the case of end-node forces and moments, the constant distributions of e_1^ε, e_4^ε, e_5^ε, and e_6^ε and the linear distributions of e_2^ε and e_3^ε can be determined, requiring a total of eight strain measurements. This number may be reduced to six by invoking the equilibrium equations of the Timoshenko beam theory which relate the bending moments (M_y, M_z) to the transverse shear forces (Q_y, Q_z)

$$\frac{\mathrm{d}M_z}{\mathrm{d}x} = Q_y \tag{12a}$$

$$\frac{\mathrm{d}M_y}{\mathrm{d}x} = Q_z. \tag{12b}$$

By using the constitutive relations of the Timoshenko beam theory,

$$\begin{aligned}
Q_y &= G_y e_5 \qquad M_y = D_y e_2\\
Q_z &= G_z e_4 \qquad M_z = D_z e_3
\end{aligned} \tag{13}$$

where $G_y \equiv k_y^2 GA$ and $G_z \equiv k_z^2 GA$ are the shear rigidities, with $k_y{}^2$ and $k_z{}^2$ denoting the shear correction factors [30, 31], and $D_y \equiv E\,I_y$ and $D_z \equiv E\,I_z$ denoting the bending rigidities, equations (12) can be written in terms of experimental transverse shear and bending section strains as

$$e_5^\varepsilon = \frac{E}{G}\frac{I_z}{k_y^2 A}e^\varepsilon_{3,x} \tag{14a}$$

$$e_4^\varepsilon = \frac{E}{G}\frac{I_y}{k_z^2 A}e^\varepsilon_{2,x}. \tag{14b}$$

It is worth noting that this procedure should be viewed as a convenient means of reducing the required number of strain gauges by solving for e_5^ε and e_4^ε analytically rather than measuring these quantities experimentally. The use of equations (15) requires knowledge of the geometry (A, I_y, I_z) and of the Poisson's ratio, ν ($E/G = 2(1 + \nu)$).

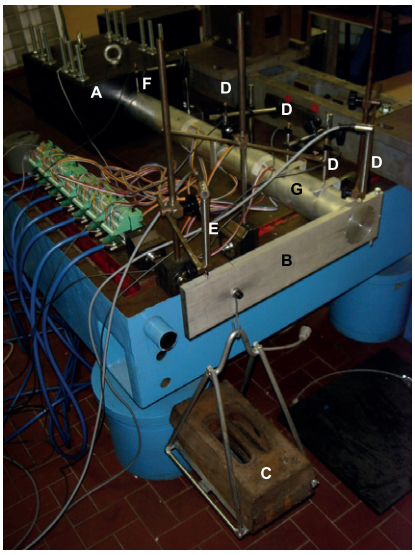

(a)

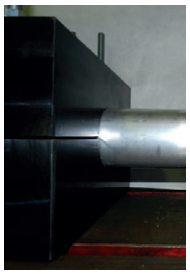

(b)

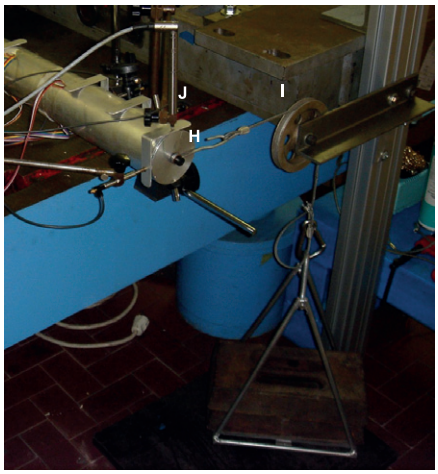

(c)

Figure 4. Static test setup. (a) A: clamping system; B: lever arm for static load case (iv); C: loading system; D: LVDT measuring deflection along the beam span; E: LVDT measuring displacement due to torsion for static load case (iv); F: LVDT measuring beam deflection at the clamped end; G: aluminum beam. (b) Clamping system (detail). (c) H: aluminum cap; I: pulley for static load case (ii); J: LVDT used to verify that the vertical displacement is negligible during static load case (ii).

3. Experimental results

Experiments were conducted at the *AERMEC* Laboratory of the Department of Mechanical and Aerospace Engineering of Politecnico di Torino in order to assess the iFEM for beam structures. The test article, shown in figure 4(a), was a thin-walled beam with a circular cross-section, with thickness $s = 1.9$ mm, external radius $R_{\text{ext}} = 40$ mm and length $\ell = 800$ mm. The material was a 6060 aluminum alloy ($E = 61\,922$ MPa, $\nu = 0.33$). The beam was mounted on a test-bed in a cantilevered configuration with one end clamped between two couples of iron blocks locked together by twelve bolted connections (figure 4(b)).

Nine stacked strain rosettes were placed at three different stations along the beam span ($x = \ell/3,\ \ell/2,\ 2\ell/3$); for each station, three rosettes were placed at $\theta = -120°,\ 0°,\ +120°$, respectively. Each rosette had three strain gauges measuring at $\beta = 0°, 45°, 90°$ (figure 3). Table 1 summarizes the strain gauge configurations used in the iFEM model (also refer to figure 5). Details of the evaluation of the section strains for each strain gauge configuration can be found in appendix B. Displacement measurements were taken at different locations along the beam span by means of linear variable differential transformers (LVDTs) and used to assess the iFEM-recovered deflections and rotations (figure 4(a)). An LVDT was also placed as close as possible to the beam root in order to verify the effectiveness of the clamping system (figure 4(a)).

3.1. Static tests

For the static tests, four different load cases were considered (figure 6):

(i) tip vertical force,
(ii) tip horizontal force,

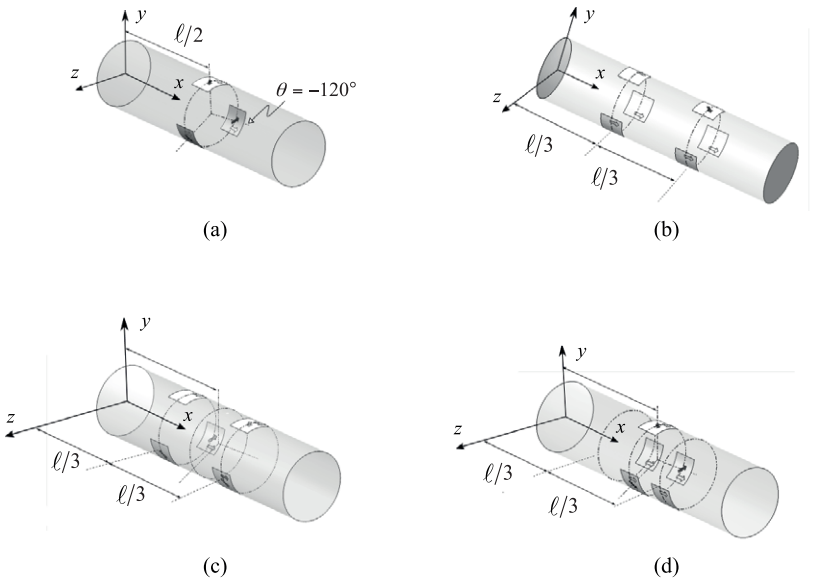

Figure 5. Schematic representation of the strain gauge configurations: C1 (a), C2 (b), C3 (c) and C4 (d).

Table 1. Description of the strain gauge configurations. For each configuration, the gauges' axial locations and orientations are reported (angles are expressed in degrees).

Notation	Description	Orientation (θ, β) at $x = \ell/3$	Orientation (θ, β) at $x = \ell/2$	Orientation (θ, β) at $x = 2\ell/3$
C1	• Six strain gauges • One axial location • Equations (12) used	—	(−120, 0), (−120, 45), (0, 0), (0, 45), (120, 0), (120, 45)	—
C2	• Six strain gauges • Two axial locations • Equations (12) used	(−120, 0), (0, 0), (120, 0)	—	(−120, 0), (0, 45), (120, 0)
C3	• Eight strain gauges • Two axial locations	(−120, 0), (−120, 45), (0, 0), (120, 45)	—	(0, 0), (0, 45), (120, 0), (120, 45)
C4	• Eight strain gauges • Three axial locations	(−120, 0)	(−120, 0), (−120, 45), (0, 0), (0, 45), (120, 0), (120, 45)	(120, 0)

(iii) tip force inclined 30° with respect to the horizontal y-axis of the cross-section,
(iv) tip vertical force applied at a distance $b = 300$ mm from the center of the cross-section.

The loading was achieved by placing several weights on a cradle (for a total weight of $F = 26.83$ kg). For cases (i), (ii), and (iii), the cradle was linked to a screw at the center of the beam tip cross-section by means of an aluminum cap embedded at the beam end (figure 4(c)), whereas, for load case (iv), the cradle was suspended from a proper lever arm provided by a thick plate embedded at the beam tip (figure 4(a)). Depending on the load case, LVDT transducers were placed at different locations along the beam span (refer to table 2). For load case (iv), the tip twist rotation was recovered by measuring the vertical displacement at two points, one in correspondence with the beam's free-end and the second at a certain distance d along the lever arm (see figure 4(a)); knowing the distance between the two LVDT transducers, d, and the difference between the two measured deflections, Δw^{LVDT}, the twist rotation of the beam free end was evaluated as $\theta_x(\ell) = \arctan(\Delta w^{\mathrm{LVDT}}/d)$. For the presented results, $d = 350$ mm. Moreover, for load cases (i), (ii) and (iv), an additional LVDT was placed at the beam tip in order to control the load direction; for example, in load case (ii) (figure 4(b)), the load has to be horizontal and a vertical LVDT was used to verify that the vertical displacement was negligible.

The accuracy of the solution is assessed by means of the percentage difference of the predicted displacements and the rotation with respect to the experimentally measured ones. The *percentage difference* is defined as

$$\%\mathrm{Diff}(\delta) = 100 \times \left[\frac{\delta^{\mathrm{iFEM}}(x_i) - \delta^{\mathrm{exp}}(x_i)}{\delta^{\mathrm{exp}}(\ell)} \right] \tag{15}$$

where $\delta = (v, w, \theta_x)$; the superscript 'iFEM' refers to the predicted value while 'exp' refers to the experimental measure;

Table 2. The experimental displacements (mm) and rotations (rad) measured using LVDTs for the static load cases.

Load case (i)					
$w(\ell/2)$	$w(3\ell/4)$	$w(7\ell/8)$	$w(\ell)$		
−0.648	−1.300	−1.635	−1.985		
Load case (ii)					
$v(\ell/2)$	$v(3\ell/4)$	$v(7\ell/8)$	$v(\ell)$		
0.636	1.272	1.648	1.994		
Load case (iii)					
$v(3\ell/4)$	$v(7\ell/8)$	$v(\ell)$	$w(3\ell/4)$	$w(7\ell/8)$	$w(\ell)$
1.098	1.414	1.667	0.644	0.802	0.963
Load case (iv)					
$w(\ell/2)$	$w(3\ell/4)$	$w(7\ell/8)$	$w(\ell)$	$\theta_x(\ell)$	
−0.664	−1.319	−1.647	−1.958	3.5×10^{-3}	

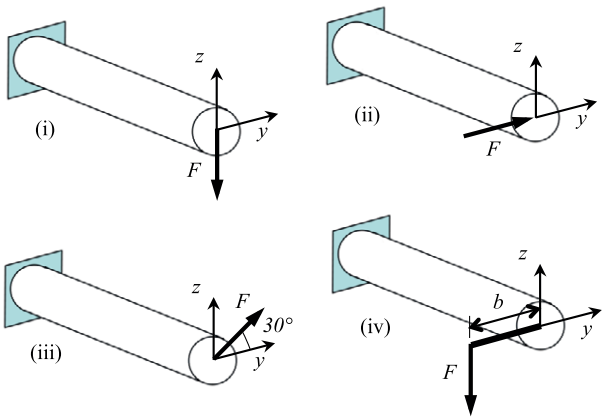

Figure 6. Static load cases.

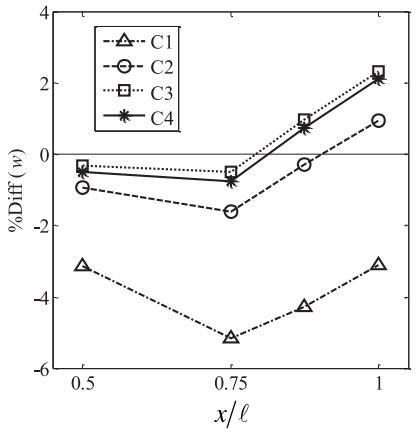

Figure 7. Percentage difference in the iFEM-predicted deflection, w, for load case (i), using a single inverse-element discretization and four different strain gauge configurations, C1–C4 (see table 1).

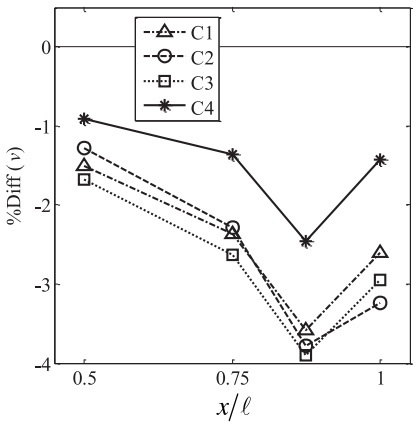

Figure 8. Percentage difference in the iFEM-predicted deflection, v, for load case (ii), using a single inverse-element discretization and four different strain gauge configurations, C1–C4 (see table 1).

x_i is the ith point along the axial coordinate where δ is measured.

At first, a single inverse element is adopted to model the entire beam. Figures 7–10 display the percentage differences of the predicted deflections, evaluated at different locations along the beam span, for load cases (i)–(iv). For each load case, results obtained with all the strain gauge configurations referred to in table 1 are compared. For load case (iv) the percentage difference in the twist rotation evaluated at $x = \ell$ is given by $\%\text{Diff}(\theta_x) = (-9.36, -5.24, -7.84, -9.36)$ for the four considered strain gauge configurations, C1–C4, respectively.

For all load cases and using any of the considered strain-gauge configurations, the iFEM-predicted tip deflections differ from the measured values by less than 7%. The inverse models that use eight strain gauges generally produce more accurate predictions compared to the six-strain gauge configurations, with the exception of case (iv) corresponding to C2 (see table 1) which produces a slightly more accurate prediction for the tip twist rotation. It is noted that the strain gauge configuration C2 has only one strain gauge rotated at 45° with respect to the beam axis ($\beta = 45°$), whereas the other configurations have at least three strain gauges along $\beta = 45°$. It may be reasonable to suppose that a strain gauge placed at $\beta = 45°$ gives a slightly less accurate measure, because of the curvature of the external beam surface. Therefore, the configuration C2 should be more

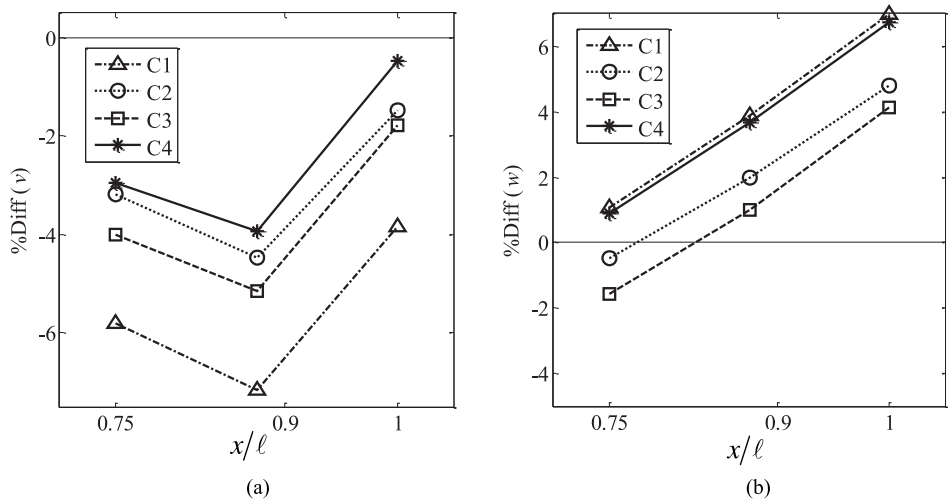

Figure 9. Percentage difference in the iFEM-predicted deflections, v (a) and w (b), for load case (iii), using a single inverse-element discretization and four different strain gauge configurations, C1–C4 (see table 1).

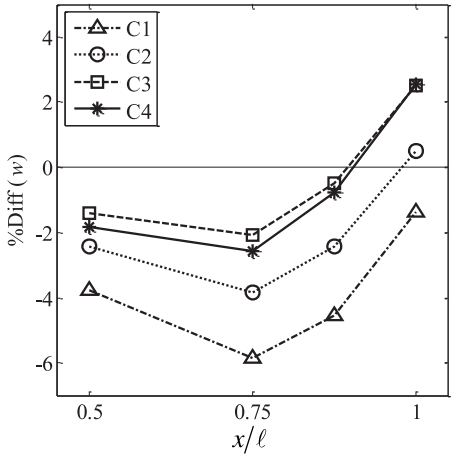

Figure 10. Percentage difference in the predicted deflection, w, for load case (iv), using a single inverse-element discretization and four different strain gauge configurations, C1–C4 (see table 1).

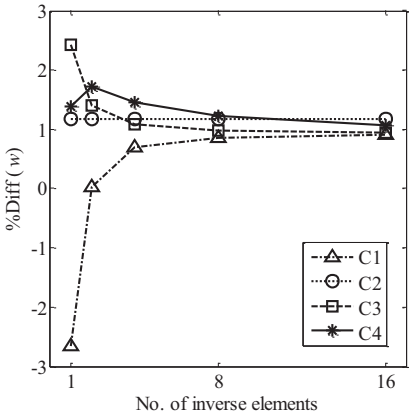

Figure 11. Percentage difference in the iFEM-predicted tip deflection, using fitted strain data, versus the number of inverse elements, for load case (i).

accurate especially for those cases where the strains measured at $\beta = 45°$ are essential. This is particularly true for load case (iv) because the strain gauges with an orientation angle of $\beta = 45°$ are the only ones measuring the strain due to torsion. Thus, for this load case, the solution is dominated by the measurement errors of the strain measured at $\beta = 45°$, and this effect is particularly evident in the twist rotation.

As a second strategy, more inverse elements are used to discretize the beam. A finer discretization of the structure would usually require a denser distribution of strain measurements. Alternatively, curve fitting can be applied to the available strain-gauge measurements to simulate experimental strain data in more locations. Following this concept, a linear function of the axial coordinate, x, is used to fit the strain values measured at $x = \ell/3,\ \ell/2,\ 2\ell/3$ for each of the considered orientations (θ, β); this yields six continuous functions of x representing the experimental evaluation of the strains at the orientation angles $(-120, 0)$, $(-120, 45)$, $(0, 0)$, $(0, 45)$, $(120, 0)$, and $(120, 45)$. Using this strategy it is possible to model the test article with as many inverse elements as needed and with all the possible strain-gauge distributions described above within each element.

Figures 11–14 summarize the results obtained for the tip displacements and rotation for each load case, using the procedure described above and an increasing number of inverse elements. The strain-gauge distribution corresponding to each curve is adopted in all the elements. As the number of inverse elements increases, the percentage difference in the predicted iFEM deflection converges to a value that is lower than 6% for all load cases. The twist angle at the beam free-end for load case (iv) is somehow less accurate; configuration C2 provides the best estimate of the twist rotation with a percentage difference of about 5.8% using 16 elements (see figure 14). The above-mentioned considerations concerning improvement in accuracy due to the C2 strain-gauge configuration apply in this case as well.

Comparing figures 7–10 with figures 11–14, some obser-vations can be made. The results presented in figures 7–10 are

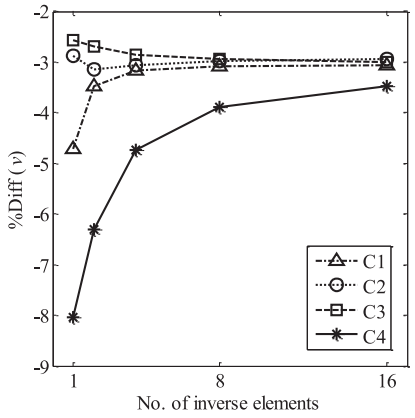

Figure 12. Percentage difference in the iFEM-predicted tip deflection, using fitted strain data, versus the number of inverse elements, for load case (ii).

obtained using measured raw-strain data, whereas in figures 11–14 every input strain is obtained by a linear fitting performed over three different values, measured at $x = \ell/3$, $\ell/2$, $2\ell/3$, respectively. As expected, the results obtained with only one inverse element are different when using the raw strain data (figures 7–10) or the fitted strain data (figures 11–14), since these data may be different at the same axial location. The major advantage of applying a fitting procedure to the raw data is that the frame member can be discretized using a large number of inverse elements without requiring the acquisition of further data. For example, a five element discretization, together with the strain gauge distribution C1, would require thirty pieces of strain data to be measured, whereas using the present strain interpolation, only eighteen are needed, independently of the number of inverse elements. This is particularly important when a more complex loading is applied, for example, a distributed load. In that case, it is advantageous to use higher-fidelity discretizations for the iFEM model. In general, the number of inverse elements to be used is related to

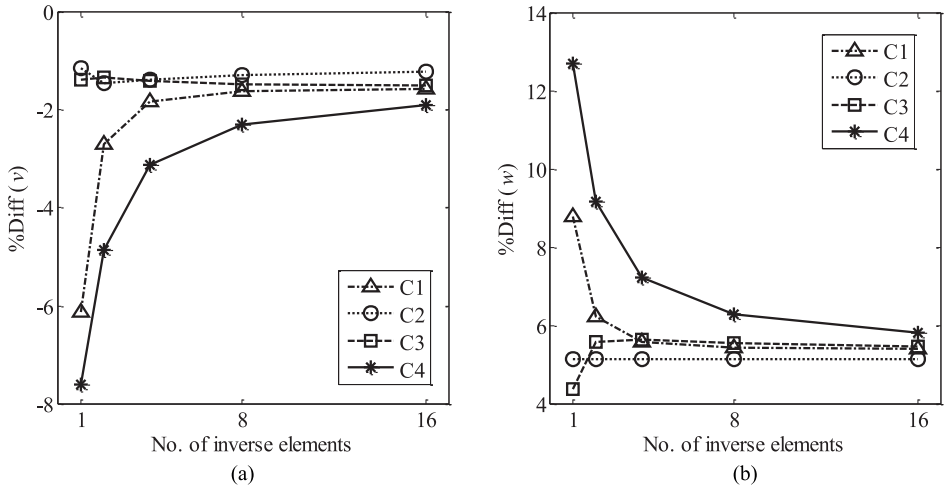

Figure 13. Percentage difference in the iFEM-predicted tip deflections, v (a) and w (b), using fitted strain data, versus the number of inverse elements, for load case (iii).

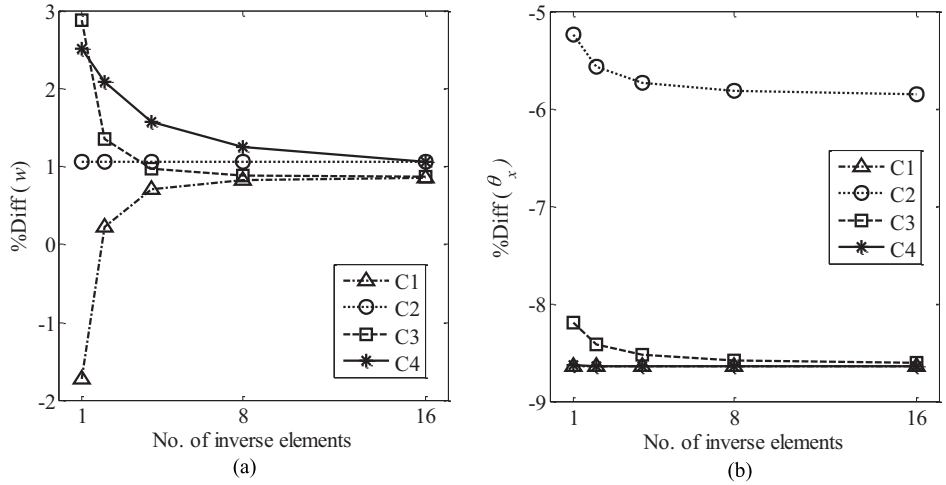

Figure 14. Percentage difference in the iFEM-predicted tip deflection (a) and twist rotation (b), using fitted strain data, versus the number of inverse elements, for load case (iv).

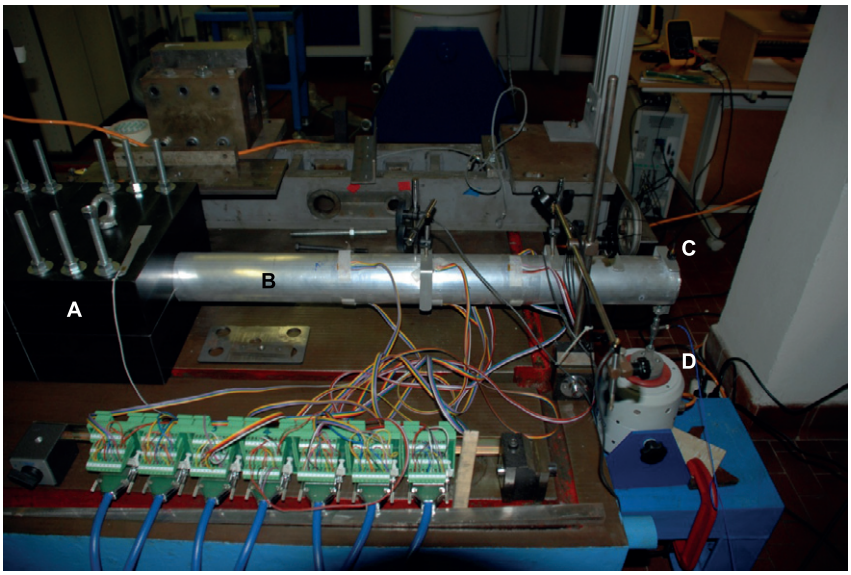

Figure 15. Dynamic test setup. A: clamping system; B: aluminum beam; C: accelerometer; D: shaker.

the complexity of the applied loading and expected structural deformations. Another important consideration is that, using the raw data, different strain-gauge configurations can lead to significantly different results (see figures 7–10), whereas using fitted data, results obtained with different strain gauge configurations converge to nearly the same values (see figures 11–14); that is, the accuracy of the solution is independent of the strain gauge configuration.

It is important to observe that the computational time is slightly affected by the number of inverse elements used, since the solution of equation (9) requires that the matrix $\mathbf{A}$ is inverted only once, whereas the remaining computation involves an extremely fast matrix–vector multiplication. In fact, most of the computational time involved in the shape reconstruction is merely due to data acquisition rather than the actual computation of the deformed shape.

An important property of the displacement field reconstruction through the iFEM is its resolution, i.e., the minimum displacement that can be evaluated using the input strain data. An estimate of the resolution is not trivial since it depends on many factors, first of all the resolution of the data acquisition system. To investigate this aspect, an experimental campaign will be conducted where a step-wise load application is adopted, the minimum measurable strain variation is recorded at each step and the corresponding reconstructed displacement field is evaluated. Since this study is not within the scope of the present paper, it will be addressed in a future work.

3.2. Dynamic tests

The same thin-walled, circular cross-section, cantilevered beam (figure 4) was used for the dynamic experiments. A harmonic vertical force was applied at the free end of the beam through a shaker rigidly linked to the screw at the center of the tip cross-section (figure 15). The displacement transducers used in the static tests were no longer operable, since they are only accurate in detecting very low-frequency motion. Thus, to verify the accuracy of the beam iFEM, a mono-axial piezoelectric accelerometer was placed at the beam free end, measuring the vertical acceleration. The trapezoidal integration rule was applied twice in order to obtain the tip vertical deflection time–history. Discrete-time integration is affected by errors that increase in time and are known as *drift* [32]; these errors result in a global linear trend in the integrated signal (parabolic trend for double integration). Furthermore, the trapezoidal rule greatly amplifies low-frequency noise, while inherently filtrating high-frequency noise [33]. Thus, in order to correct the integrated displacement, a high-pass Butterworth filter was used after integration [32]; to obtain zero-phase filtering, the filter was applied twice to the signal in the forward and backward directions [34]. The filter design and filtering operations were achieved by using available functions of the commercial code MATLAB$^{\bigcirc R}$ R2007a. In order to suppress high-frequency noise that affects the strain gauge measurements, a low-pass filter was applied to the measured strains. Moreover, to keep the phase unshifted, double forward–backward filtering was applied to the strain gauge measured signals. A sixth-order Butterworth filter was designed again using MATLAB $^{R\bigcirc}$ R2007a functions (cut-off frequency equal to 200 Hz).

Using a harmonic vertical force, $F = F_0 \sin(2\pi f_0 t)$, two different tests were conducted:

(a) at $f_0 = 10$ Hz with $F_0 = 70$ N;
(b) at $f_0 = 40$ Hz with $F_0 = 80$ N.

In both tests, f_0 was lower than the fundamental frequency of the beam, i.e. approximately 130 Hz, as predicted by a high-fidelity FEM modal analysis of the test article conducted with MSC/NASTRAN$^{\bigcirc R}$ [29]. In figures 16 and 17 the tip's vertical displacement evaluated using one inverse finite element and the strain gauge configuration C2 of table 1 is compared

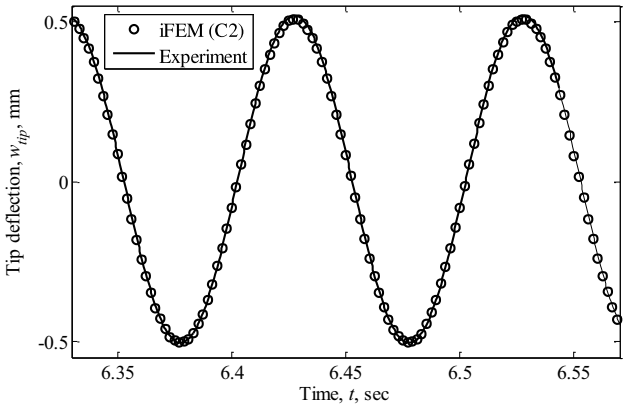

Figure 16. Tip deflection of the beam loaded by a harmonic force (frequency 10 Hz and amplitude 70 N).

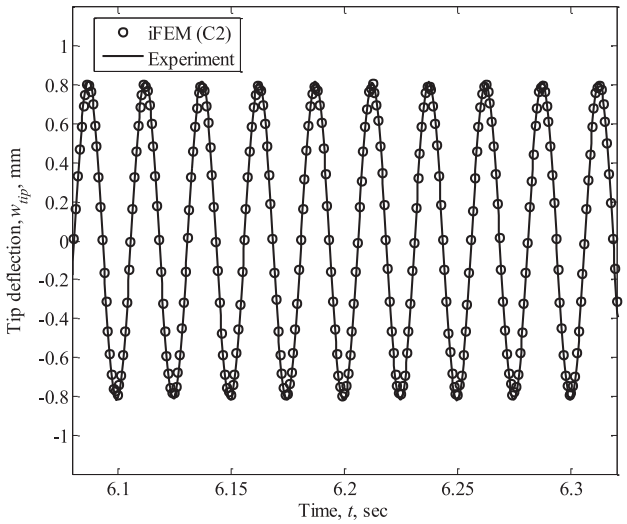

Figure 17. Tip deflection of the beam loaded by a harmonic force (frequency 40 Hz and amplitude 80 N).

with the twice-integrated accelerometer signal for the two excitation frequencies. Taking only maximum or minimum values in the sinusoidal response obtained by the accelerometer measurement, the largest iFEM percentage differences, for the given time histories, are summarized in table 3. The percentage differences are calculated as follows:

$$\%\mathrm{Diff}(w) = 100 \times \left[\frac{w^{\mathrm{iFEM}}(\ell)}{w^{\mathrm{exp}}(\ell)} - 1 \right] \tag{16}$$

where $w^{\mathrm{exp}}(\ell)$ is obtained from integration of the accelerometer signal.

The results of the dynamic experimental assessment of the iFEM for beams confirm the accuracy and efficiency of the present formulation, particularly taking into account that only a single inverse element has been used to model the beam. Naturally, modeling of more complex deformations associated with the higher-frequency regime would require a higher-fidelity discretization for the iFEM model. In this case, more strain measurements would have to be acquired or, as discussed in section 3.1, a suitable polynomial fitting would have to be applied to the raw strain data. Thus, a higher-fidelity discretization would result in larger matrices; nevertheless, the computation remains extremely efficient using the matrix–vector multiplication $\mathbf{A}^{-1}\,\mathbf{b}$, where only the values in the $\mathbf{b}$ vector will change for different time/strain evaluations.

Table 3. Percentage difference of iFEM-predicted maximum/minimum tip deflection.

Load, F	Frequency, f_0 (Hz)	10	40
	Force magnitude, F_0 (N)	70	80
%Diff (w)	C1	**−3.16**	**−5.89**
	C2	**−2.00**	**−3.36**
	C3	**3.95**	**2.19**
	C4	**3.54**	**−5.21**

4. Conclusions

Shape sensing is an inverse problem aiming at the reconstruction of the three-dimensional displacement field of a structure from strains measured at discrete locations on its surface. An inverse finite element method (iFEM) has been presented in this paper for the shape sensing of beam and frame structures based on Timoshenko's kinematic assumptions. The methodology is based on a least-squares functional which is discretized by C^0-continuous displacement-based *inverse* frame elements. The variational statement enforces least-square compatibility between the experimentally measured strains due to stretching, torsion, bending and transverse shear, and those interpolated within the inverse elements.

The fundamentals of the iFEM have been briefly reviewed to set the framework for an assessment of the methodology when used with experimental strain data. A thin-walled cantilevered beam has been subjected to static and dynamic loads in a mechanics laboratory. Strains measured by surface-mounted strain gauges have been employed in the shape-sensing analyses. Displacement transducers and accelerometers have been used to measure the beam's response, with these measurements used to verify the accuracy of the iFEM reconstructed displacements.

With the use of a single inverse element, the iFEM-reconstructed displacements and rotations compared favorably with those measured experimentally. When the beam was discretized with multiple elements, a convergent trend of the results towards the experimentally measured displacements and rotations was demonstrated. The number and the distribution of strain gauges have also been shown to influence the accuracy of the iFEM predictions. The studies have demonstrated the robustness of the approach with respect to unavoidable measurement errors due to strain-gauge location, measurement systems, and geometric imperfections.

The results of this work point towards the possibility of determining optimally distributed locations of the strain gauges in order to achieve further improvements in the shape-sensing predictions. Moreover, further benefits to the accuracy and robustness of the methodology can be achieved

by the use of distributed strain-measurement techniques, e.g., fiber Bragg grating (FBG) sensors. The proposed inverse finite element method represents a powerful tool for both shape sensing and health monitoring of smart structures that are instrumented with embedded strain-sensing systems.

Acknowledgments

The authors gratefully acknowledge the fundamental contribution to the experimental activity by Mr Giuseppe Ruvinetti of Politecnico di Torino. The authors also acknowledge Daniela Laschera and Fabio Zito for their help during the experimental activity which was part of their thesis activity for a degree in Aerospace Engineering.

Appendix A

The first- and second-degree Lagrange shape functions are given as follows:

$$\begin{aligned}[L_1^{(1)},\ L_2^{(1)}] &\equiv \tfrac{1}{2}[(1-\xi),\ (1+\xi)] \\ [L_1^{(2)}, L_r^{(2)}, L_2^{(2)}] &\equiv \tfrac{1}{2}[\xi(\xi-1), 2(1-\xi^{(2)}), \xi(\xi+1)]\end{aligned} \tag{A.1}$$

where $\xi \equiv 2x/\ell^e - 1 \in [-1, 1]$ is a non-dimensional axial coordinate; $x \in [0, \ell^e]$ and ℓ^e denotes the element length. The subscripts 1 and 2 are labels representing the end nodes, r denotes the middle node.

The third-degree shape functions, $N_j^{(3)}(\xi)$, have the form

$$\begin{aligned}[N_1^{(3)}, N_r^{(3)}, N_2^{(3)}] \equiv \frac{\ell^e}{24}(1-\xi^{(2)}) \\ \times\ [(2\xi-3), -4\xi, (2\xi+3)].\end{aligned} \tag{A.2}$$

Appendix B

For each strain-gauge configuration, the sections' strains are evaluated at $x_i = \ell/3$ and $x_i = 2\ell/3$ as follows.

(*C1*) The strain-gauge configuration C1 consists of six strain gauges located at $x_i = \ell/2$. By writing equation (11) for each measured strain, the section strains are evaluated at the beam mid-span, $e_k^{\varepsilon}(\ell/2)$, $k = 1, \ldots, 6$. Thus, remembering that the bending section strains e_2^{ε} and e_3^{ε} are assumed to be linear and evaluating their derivatives, $e_{2,x}^{\varepsilon}$ and $e_{3,x}^{\varepsilon}$, at $x_i = \ell/2$ by means of equation (15), the values of e_2^{ε} and e_3^{ε} can be easily estimated at $x_i = \ell/3$ and $2\ell/3$. As e_1^{ε}, e_4^{ε}, e_5^{ε} and e_6^{ε} are supposed to be constant, their values along the beam span are assumed to be the same as at $x_i = \ell/2$.

(*C2*) For the strain-gauge configuration C2, equation (11) gives rise to six equations—one for each strain-gauge measurement—with eight unknowns: the constant section strains e_1^{ε}, e_4^{ε}, e_5^{ε} and e_6^{ε}, and two values for each of the linear strain measures, $e_j^{\varepsilon}(\ell/3)$ and $e_j^{\varepsilon}(2\ell/3)$, $j = 2, 3$. The system can be solved by adding the following two equations:

$$\frac{3}{\ell}(e_j^{\varepsilon}(2\ell/3) - e_j^{\varepsilon}(\ell/3)) = e_{j,x}^{\varepsilon} \qquad (j = 2, 3) \tag{B.1}$$

where the derivatives $e_{2,x}^{\varepsilon}$ and $e_{3,x}^{\varepsilon}$ are given by equa-tion (15).

(*C3*) Equation (11) is written eight times, thus enabling the evaluation of the eight unknowns, e_1^{ε}, e_4^{ε}, e_5^{ε} and e_6^{ε}, and $e_j^{\varepsilon}(\ell/3)$ and $e_j^{\varepsilon}(2\ell/3)$, $j = 2, 3$.

(*C4*) By writing equation (11) for each of the eight strain gauges, we introduce ten unknowns: e_1^{ε}, e_4^{ε}, e_5^{ε} and e_6^{ε}, and $e_j^{\varepsilon}(\ell/3)$, $e_j^{\varepsilon}(\ell/2)$ and $e_j^{\varepsilon}(2\ell/3)$, $j = 2, 3$. Then, in order to solve this problem, the following relationships can be written:

$$\frac{e_j^{\varepsilon}(\ell/3) + e_j^{\varepsilon}(2\ell/3)}{2} = e_j^{\varepsilon}(\ell/2) \qquad (j = 2, 3) \tag{B.2}$$

where we use the assumption that the bending curvatures are linear along the element span.

References

[1] Hopkins M A, Truss J M, Lockyer A J, Alt K, Kinslow R and Kudva J N 1997 Smart skin conformal load bearing antenna and other smart structures developments *Proc. 38th AIAA/ASME/ASCE/AHS/ASC Structures, Structural Dynamics and Materials Conf. (Kissimmee, FL, April 1997)* pp 521–530

[2] Yin W, Fu T, Liu J and Leng J 2009 Structural shape sensing for variable camber wing using FBG sensors *Proc. SPIE* **7292** 72921H

[3] Akl W, Poh S and Baz A 2007 Wireless and distributed sensing of the shape of morphing structures *Sensors Actuators* A **140** 94–102

[4] Bruno R, Toomarian N and Salama M 1994 Shape estimation from incomplete measurements: a neural-net approach *Smart Mater. Struct.* **3** 92–7

[5] Mao Z and Todd M 2008 Comparison of shape reconstruction strategies in a complex flexible structure *Proc. SPIE* **6932** 69320H

[6] Arritt B, Murphey T, Dumm H-P, Pollard E and Klimcak C 2007 Demonstration of the use of fiber-optics, with Integrated Fiber-Bragg Gratings, for shape determination of large deployable structures *Proc. 48th AIAA/ASME/ASCE/AHS/ASC Structures, Structural Dynamics, and Materials Conf. (Honolulu, HI, April 2007)* AIAA 2007-2006

[7] Tessler A and Spangler J L 2005 A least-squares variational method for full-field reconstruction of elastic deformations in shear-deformable plates and shell *Comput. Methods Appl. Mech. Eng.* **194** 327–39

[8] Foss G and Haugse E 1995 Using modal test results to develop strain to displacement transformations *Proc. 13th Int. Conf. Modal Anal.* (Nashville, TN, Feb. 1995) pp 112–118

[9] Lively P S, Atalla M J and Hagood N W 2001 Investigation of filtering techniques applied to the dynamic shape estimation problem *Smart Mater. Struct.* **10** 264–72

[10] Glaser R, Caccese V and Shahinpoor M 2012 Shape monitoring of a beam structure from measured strain or curvature *Exp. Mech.* **52** 591–606

[11] Davis M A, Kersey A D, Sirkis J and Friebele E J 1996 Shape and vibration mode sensing using a fiber optic Bragg grating array *Smart Mater. Struct.* **5** 759–65

[12] Todd M D and Vohra S T 1999 Shear deformation correction to transverse shape reconstruction from distributed strain measurements *J. Sound Vib.* **225** 581–94

[13] Bogert P B, Haugse E D and Gehrki R E 2003 Structural shape identification from experimental strains using a modal transformation technique *Proc. 44th AIAA/ASME/ASCE/AHS Structures, Structural Dynamics and Materials Conf. (Norfolk, VA, 2003)* AIAA 2003-1626

[14] Rapp S, Kang L-H, Han J-H, Mueller U C and Baier H 2009 Displacement field estimation for a two-dimensional structure using fiber Bragg grating sensors *Smart Mater. Struct.* **18** 025006

[15] Kim H-I, Kang L-H and Han J-H 2011 Shape estimation with distributed fiber Bragg grating sensors for rotating structures *Smart Mater. Struct.* **20** 035011

[16] Kim N S and Cho N S 2004 Estimating deflection of a simple beam model using fiber optic Bragg-grating sensors *Exp. Mech.* **44** 433–9

[17] Ko W L, Richards W L and Fleischer V T 2009 Applications of the Ko displacement theory to the deformed shape predictions of the doubly-tapered Ikhana wing *NASA Technical Paper* NASA/TP-2009-214652

[18] Jones R T, Bellemore D G, Berkoff T A, Sirkis J S, Davis M A, Putnam M A, Friebele E J and Kersey A D 1998 Determination of cantilever plate shapes using wavelength division multiplexed fiber Bragg grating sensors and a least-squares strain-fitting algorithm *Smart Mater. Struct.* **7** 178–88

[19] Mainc¸on P 2004 Inverse FEM I: load and response estimates from measurements *Proc. 2nd Int. Conf. on Structural Engineering, Mechanics and Computation (Cape Town, 2004)* pp 967–71

[20] Mainc¸on P 2004 Inverse FEM II: dynamic and non-linear problems *Proc. 2nd Int. Conf. on Structural Engineering, Mechanics and Computation (Cape Town, 2004)* pp 991–5

[21] Nishio M, Mizutani T and Takeda N 2010 Structural shape reconstruction with consideration of the reliability of distributed strain data from a Brillouin-scattering-based optical fiber sensor *Smart Mater. Struct.* **19** 1–14

[22] Vazquez S L, Tessler A, Quach C C, Cooper E G, Parks J and Spangler J L 2005 Structural health monitoring using high-density fiber optic strain sensor and inverse finite element methods *NASA Technical Paper* NASA/TM-2005–213761

[23] Quach C C, Vazquez S L, Tessler A, Moore J P, Cooper E G and Spangler J L 2005 Structural anomaly detection using Element Method fiber optic sensors and inverse Finite *Proc. AIAA Guidance, Navigation, and Control Conf. (San Francisco, CA, 2005)*

[24] Gherlone M 2008 Beam inverse finite element formulation *LAQ Report* Politecnico di Torino

[25] Cerracchio P, Gherlone M, Mattone M, Di Sciuva M and Tessler A 2010 Shape sensing of three-dimensional frame structures using the inverse finite element method *Proc. 5th European Workshop on Structural Health Monitoring (Sorrento, 2010)* pp 615–20

[26] Gherlone M, Cerracchio P, Mattone M, Di Sciuva M and Tessler A 2011 Dynamic shape reconstruction of three-dimensional frame structures using the inverse finite element method *Proc. 3rd ECCOMAS Thematic Conf. on Computational Methods in Structural Dynamics and Earthquake Engineering (Corf˙u, 2011)*

[27] Gherlone M, Cerracchio P, Mattone M, Di Sciuva M and Tessler A 2011 Dynamic shape reconstruction of three-dimensional frame structures using the inverse finite element method *NASA Technical Paper* NASA/TP-2011-217315

[28] Gherlone M, Cerracchio P, Mattone M, Di Sciuva M and Tessler A 2011 Beam shape sensing using inverse finite element method: theory and experimental validation *Proc. 8th Int. Workshop on Structural Health Monitoring (Stanford, CA, Sept. 2011)*

[29] Gherlone M, Cerracchio P, Mattone M, Di Sciuva M and Tessler A 2012 Shape sensing of 3D frame structures using an inverse finite element method *Int. J. Solids Struct.* **49** 3100–12

[30] Timoshenko S P 1921 On the correction for shear of differential equations for transverse vibrations of prismatic bars *Phil. Mag.* **41** 744–6

[31] Cowper G R 1966 The shear coefficient in Timoshenko's beam theory *J. Appl. Mech.* **33** 335–40

[32] Latt W T, Veluvolu K C and Ang W T 2011 Drift-free position estimation of periodic or quasi-periodic motion using inertial sensors *Sensors* **11** 5931–51

[33] Smyth A and Wu M 2007 Multi-rate Kalman filtering for the data fusion of displacement and acceleration response measurements in dynamic system monitoring *Mech. Syst. Signal Process.* **21** 706–23

[34] Oppenheim A V and Schafer R W 1989 *Discrete-Time Signal Processing* (New York: Prentice-Hall)